

Application of 3D U-Net Neural Networks in Extracting the Epoch of Reionization Signal from SKA-Low Observations Based on Real Observations of NCP Field from LOFAR

LI-YANG GAO ^{1,2}, LÉON V. E. KOOPMANS ², FLORENT G. MERTENS ^{2,3}, SATYAPAN MUNSHI ², YICHAO LI ¹,
STEFANIE A. BRACKENHOFF ², EMILIO CECCOTTI ^{2,4}, J. KARIUKI CHEGE ², ANSHUMAN ACHARYA ⁵,
RAGHUNATH GHARA ⁶, SAMBIT K. GIRI ⁷, ILIAN T. ILIEV ⁸, GARRELT MELLEMA ⁹, AND XIN ZHANG ^{1,10,11}

¹Liaoning Key Laboratory of Cosmology and Astrophysics, College of Sciences, Northeastern University, Shenyang 110819, China

²Kapteyn Astronomical Institute, University of Groningen, P.O. Box 800, 9700 AV Groningen, the Netherlands

³LERMA, Observatoire de Paris, Université PSL, CNRS, Sorbonne Université, F-75014 Paris, France

⁴INAF – Istituto di Radioastronomia, Via P. Gobetti 101, 40129 Bologna, Italy

⁵Max-Planck-Institut für Astrophysik, Garching 85748, Germany

⁶Department of Physical Sciences, Indian Institute of Science Education and Research Kolkata, Mohanpur, WB 741246, India

⁷Van Swinderen Institute for Particle Physics and Gravity, University of Groningen, Nijenborgh 4, 9747 AG Groningen, The Netherlands

⁸Department of Physics & Astronomy, University of Sussex, Brighton, BN1 9QH, UK

⁹Dept. of Astronomy & Oskar Klein Centre, Stockholm University, AlbaNova, Stockholm University, SE-106 91 Stockholm, Sweden

¹⁰MOE Key Laboratory of Data Analytics and Optimization for Smart Industry, Northeastern University, Shenyang 110819, China

¹¹National Frontiers Science Center for Industrial Intelligence and Systems Optimization, Northeastern University, Shenyang 110819, China

ABSTRACT

Neutral hydrogen (HI) serves as a crucial probe for the Cosmic Dawn and the Epoch of Reionization (EoR). Actual observations of the 21-cm signal often encounter challenges such as thermal noise and various systematic effects. To overcome these challenges, we simulate SKA-Low-depth images and process them with a deep learning method. We utilized foreground residuals acquired by LOFAR during actual North Celestial Pole (NCP) field observations, thermal and excess variances calculated via Gaussian process regression (GPR), and 21-cm signals generated with **21cmFAST** for signal extraction tests. Our approach to overcome these foreground, thermal noise, and excess variance components employs a 3D U-Net neural network architecture for image analysis. When considering thermal noise corresponding to 1400 hours of integration, U-Net provides reliable 2D power spectrum predictions, and robustness tests ensure that we get realistic EoR signals. Adding foreground residuals, however, causes inconsistencies below the horizon delay-line. Lastly, evaluating both thermal and excess variance with observations up to 3700 and 14000 hours ensures reliable power spectrum estimations within the EoR window and across nearly all scales, respectively.

Keywords: H I line emission(690) — Reionization(1383) — Gaussian Processes regression(1930) — Neural networks(1933)

1. INTRODUCTION

To fully explore the Cosmic Dawn (CD, Pritchard & Furlanetto 2007) ($12 < z < 30$) and the Epoch of Reionization (EoR, Madau et al. 1997) ($6 < z < 12$), there is a need for a new probe of the infant Universe, beyond infrared observations with the James Webb Space Telescope (JWST), Hubble Space Telescope (HST), and (sub-)mm observations with the Atacama Large Millimeter/submillimeter

Array (ALMA), which only probe the brightest galaxies at these early epochs. The 21-cm signal is regarded as the most promising probe for detecting the distribution of neutral hydrogen (HI) in the inter-galactic medium (IGM) during the CD and the EoR (Madau et al. 1997; Shaver et al. 1999; Furlanetto et al. 2006; Pritchard & Loeb 2012; Zaroubi 2013), which can help us understand the formation of the first generation of stars as well as galaxies and the evolution of the infant universe.

Because the instruments of current generation do not have the sensitivity to make direct images of the HI distribution during the EoR, the 21-cm signal is mainly characterized by its power spectrum. Many currently employed and up-

coming experiments aim to observe and constrain the 21-cm signal during the CD and the EoR. In [Paciga et al. \(2013\)](#), the Giant Metrewave Radio Telescope¹ (GMRT, [Ananthkrishnan 1995](#)) Epoch of Reionization experiment reported $\Delta_{21}^2 < (248)^2 \text{mK}^2$ at $k = 0.50 \text{ h cMpc}^{-1}$ and $z \approx 8.6$ in the 21-cm power spectrum. The latest 5.5-hours observation from the Murchison Widefield Array² (MWA, [Barry et al. 2019](#); [Li et al. 2019](#); [Trott et al. 2020](#)) reported $\Delta_{21}^2 < 6.3 \times (10)^2 \text{mK}^2$ at $k = 0.14 \text{ h cMpc}^{-1}$ and $z \approx 15.2$ in the 21-cm power spectrum in [Yoshiura et al. \(2021\)](#). Using a 4-hour observation from the Owen’s Valley Radio Observatory - Long Wavelength Array³ (OVRO-LWA, [Eastwood et al. 2019](#)), [Garsden et al. \(2021\)](#) reported an upper limit of $\Delta_{21}^2 < 2 \times (10)^{12} \text{mK}^2$ at $k = 0.3 \text{ h cMpc}^{-1}$ and $z = 28$ on the 21-cm power spectrum. [Mertens et al. \(2020\)](#) achieved a 2σ upper limit on the 21-cm power spectrum of $\Delta_{21}^2 < (73)^2 \text{mK}^2$ at $k = 0.075 \text{ h cMpc}^{-1}$ and $z \approx 9.1$ for the Low-Frequency Array⁴ (LOFAR, [van Haarlem et al. 2013](#); [Gehlot et al. 2019, 2020](#)) based on ten nights of observations of the North Celestial Pole (NCP) field ([Yatawatta et al. 2013](#); [Patil et al. 2017](#)). New Extension in Nançay Upgrading LOFAR⁵ (NenuFAR) set a 2σ upper limit of $\Delta_{21}^2 < 2.4 \times (10)^7 \text{mK}^2$ at $k = 0.041 \text{ h cMpc}^{-1}$ and $z = 20.3$ on the 21-cm power spectrum from one-night observation in [Munshi et al. \(2024a\)](#).

For second-generation experiments, the Hydrogen Epoch of Reionization Array⁶ (HERA, [DeBoer et al. 2017](#)) Phase I gave the first results: two 2σ upper limits of $\Delta_{21}^2 < (30.76)^2 \text{mK}^2$ at $k = 0.192 \text{ h cMpc}^{-1}$ and $z = 7.9$ and $\Delta_{21}^2 < (95.74)^2 \text{mK}^2$ at $k = 0.256 \text{ h cMpc}^{-1}$ and $z = 10.4$ with one 36-hour observation. HERA Phase II and Square Kilometer Array - Low⁷ (SKA-Low, [Koopmans et al. 2015](#)) are expected to have longer baselines and higher sensitivity, so we will have better constraints on the HI power spectrum and even get HI sky maps in the CD and the EoR.

However, there are still many difficulties in extracting the 21-cm signal. During CD and EoR, the intensity of the foreground ([Cunnington et al. 2021](#); [Spinelli et al. 2021](#); [Wolz et al. 2015](#)) is orders of magnitude higher than the intensity of the 21-cm signal. Therefore, if we do not subtract the foreground carefully, the signal will be buried by foreground residuals, or the subtraction results in significant signal loss. In addition to this, the foreground is affected by chromatic instrumental effects ([Matshawule et al. 2021a](#)) such as beam

effects and polarization leakage ([Nunhokee et al. 2017](#); [Bhatnagar & Nityananda 2001](#)). Due to the smooth frequency dependence of the foregrounds, however, there are ways to separate them from the faint 21-cm signal ([Bowman et al. 2009](#); [Ansari et al. 2012](#); [Chapman et al. 2012](#)). Principal component analysis (PCA, [Masui et al. 2013](#)), fast independent component analysis (FASTICA, [Chapman et al. 2012](#); [Cunnington et al. 2019](#); [Wolz et al. 2014](#); [Hyvarinen 1999](#)), and generalized morphological component analysis (GMCA, [Bobin et al. 2007](#)) are mostly used for blind foreground subtraction. For nonblind foreground subtraction, multiple steps such as Radio Frequency Interference (RFI) mitigation, calibration, sky modeling, and subtraction of sources with applied calibration solution are required to subtract the foreground. We will briefly describe these steps further below in Section 2.1.1.

Thermal noise also affects the extraction of 21-cm signals. Without sufficient integration time, a low signal-to-noise ratio (S/N) can still result in an unobservable 21-cm signal. Observing the structure of the early universe means that we need a very long integration time in combination with a large collecting area on short baselines.

Instrumental effects, inherent in all radio telescope systems, significantly increase the challenges and complexity, associated with traditional component separation techniques. Elements such as antenna primary beam sidelobes ([Matshawule et al. 2021b](#)) and polarization leakage ([Cunnington et al. 2021](#); [Asad et al. 2015, 2016, 2018](#)) considerably complicate the foreground spectra. During actual LOFAR observations, distinguishing among these individual components is difficult ([Mertens et al. 2020](#)).

To solve the problems mentioned above in the observations, we will process the images using a deep learning approach. Inspired by [Makinen et al. \(2021\)](#), we used the 3D U-Net architecture to deal with the polarization leakage ([Gao et al. 2023](#)) and the beam effect ([Ni et al. 2022](#)) in low-redshift observations in previous works. Moreover, several studies which focused on SKA have already given promising outcomes ([Bianco et al. 2021, 2024a](#); [Chen et al. 2024](#); [Bianco et al. 2024b](#)). To enhance the realism of the images and the credibility of the results, we will evaluate this deep learning approach using SKA mock thermal noise, excess variance, and foreground residuals derived from a real LOFAR observation in the NPC field during the Epoch of Reionization.

In this paper, we present the simulation of images for each component and their subsequent processing in Section 2, the deep learning methodology in Section 3, the results along with the discussions in Section 4, and conclusion in Section 5.

2. SIMULATION

¹ <https://www.gmrt.ncra.tifr.res.in/>

² <https://www.mwatelescope.org/>

³ <https://www.ovro.caltech.edu/>

⁴ <http://www.lofar.org/>

⁵ <https://nenufar.obs-nancay.fr/en/homepage-en/>

⁶ <https://reionization.org/>

⁷ <https://www.skao.int/>

Because the NCP field is visible every night throughout the year with LOFAR, it serves as an excellent EoR window. To enhance the realism of the simulation, this study focuses on the analysis of the $4^\circ \times 4^\circ$ field of NCP as observed by the LOFAR EoR Key Science Project using the High-Band Antenna (HBA) system. All simulations in this paper are based on LOFAR observations for the NCP field, including instrument observational capabilities, the effect of the bright compact radio source 3C61.1 in the NCP field, and the mask of uv-coverage. We consider two observations, all scenarios with LOFAR and SKA-Low, respectively. The core SKA-Low site is located in Australia within the southern hemisphere, so its observing field is predominantly in the southern sky. However, to understand SKA’s observational capabilities, we assume that SKA also observes an NCP-like sky field and has the same mask of uv-coverage as LOFAR to ensure a realistic scenario, but with a much lower thermal noise for the same observing time. The imaging capabilities and sensitivity of LOFAR⁸ and SKA-Low (Barry et al. 2021) are taken into account in the simulation of thermal noise and excess variance, which we also scale to various levels to assess their impacts on the 21-cm signal reconstructions. Owing to the still-limited observational depth of LOFAR, this study presents its constraint results in the appendix A and B. Our primary focus in this research is on reconstructing the 21-cm signal from SKA-Low in a scenario where both thermal and excess variance are present but at levels considerably below that of the current LOFAR levels.

2.1. Foreground residual

The simulation of the foreground residuals is first based on LOFAR’s real observations in the NCP field. Based on the foreground residuals obtained after pipelining the raw data by LOFAR, we simulated the smooth SKA foreground residuals using a Gaussian process.

2.1.1. LOFAR-EoR pipeline

The foreground residuals were obtained as documented in Mertens et al. (2020). We acquired the unsubtracted NCP observation over 141 hours of data collected in LOFAR Cycles 0, 1, 2, and 3, employing all core stations in split mode (effectively totaling 48 stations) and including remote stations. The distribution of LOFAR stations determines the uv-coverage as a function of frequency. We concentrate on the 134 – 146 MHz frequency range (redshift bin $z \approx 8.7 - 9.6$). Processing the actual observed signal involves a complex series of steps. Following the LOFAR-EoR pipeline, the procedure starts with RFI excision, direction-independent (DI) calibration, and direction-dependent (DD) calibration, which in-

volves the subtraction of the sky model and subsequent imaging. This process ultimately produces the foreground residual images of the NCP as a function of frequency. For further details on the procedure, see Mertens et al. (2020); Patil et al. (2017). The uv-coverage is limited to 50 – 250 λ baselines. It should be noted that the flagging of the residuals of CasA and CygA resulted in a cross pattern on the uv-coverage as shown in Fig. 1. Finally, we use Gaussian process regression (GPR) to obtain the pure foreground residual.

2.1.2. Gaussian process regression

Gaussian process (GP) is a non-parametric Bayesian method for modeling functions distributed on a continuous input space (Rasmussen & Williams 2005; Gelman et al. 2013). A GP can be defined as a set of random variables or vectors where the joint distribution of each subset is a multivariate Gaussian distribution,

$$\mathbf{f}(\mathbf{x}) \sim \mathcal{GP}(m(\mathbf{x}), \mathbf{K}(\mathbf{x}, \mathbf{x}')), \quad (1)$$

where \mathbf{x} are the points in some continuous input space, $m(\mathbf{x})$ is the mean value of \mathbf{x} , and $\mathbf{K}(\mathbf{x}, \mathbf{x}')$ is the corresponding covariance matrix which is also called “kernel”. And finally we can get the joint distribution of all these random variables $\mathbf{f}(\mathbf{x})$.

After processing using the LOFAR-EoR pipeline as described above, we obtain the gridded visibility data cube $\tilde{T}(u, v, \nu)$. The data \mathbf{d} can be viewed as the sum of multiple components, i.e., foreground \mathbf{f}_{fg} , excess variance \mathbf{f}_{ex} , thermal noise $\mathbf{n}(\nu)$, and 21-cm EoR signal \mathbf{f}_{21} ,

$$\mathbf{d} = \mathbf{f}_{\text{fg}}(\nu) + \mathbf{f}_{\text{ex}}(\nu) + \mathbf{f}_{21}(\nu) + \mathbf{n}(\nu). \quad (2)$$

All GP components are functions of frequency ν . Since each component has different spectral behavior, we can theoretically distinguish them by the different kernels of the GPR. The covariance matrix $\mathbf{K}(\nu_p, \nu_q)$ for the entire data set can be written as

$$\mathbf{K}(\nu_p, \nu_q) = \mathbf{K}_{\text{fg}}(\nu_p, \nu_q) + \mathbf{K}_{\text{ex}}(\nu_p, \nu_q) + \mathbf{K}_{\text{ns}}(\nu_p, \nu_q) + \mathbf{K}_{21}(\nu_p, \nu_q). \quad (3)$$

The foreground is primarily due to diffuse Galactic emissions and extragalactic point sources. The excess variance represents additional power in the data with a small coherence scale, making it challenging to distinguish from the 21-cm signal, often arising from systematic errors. Noise is generated from thermal emissions within antennas, receivers, and related apparatus. The 21-cm signal is emitted from neutral hydrogen during reionization. $\mathbf{K}_{\text{fg}}(\nu_p, \nu_q)$ and $\mathbf{K}_{\text{ex}}(\nu_p, \nu_q)$ follow the Matern class functions,

$$\kappa_{\text{Matern}}(\nu_p, \nu_q) = \sigma^2 \frac{2^{1-\eta}}{\Gamma(\eta)} \left(\frac{\sqrt{2\eta}r}{l} \right)^\eta K_\eta \left(\frac{\sqrt{2\eta}r}{l} \right). \quad (4)$$

⁸ <https://science.astron.nl/telescopes/lofar/lofar-system-overview/observing-modes/lofar-imaging-capabilities-and-sensitivity/>

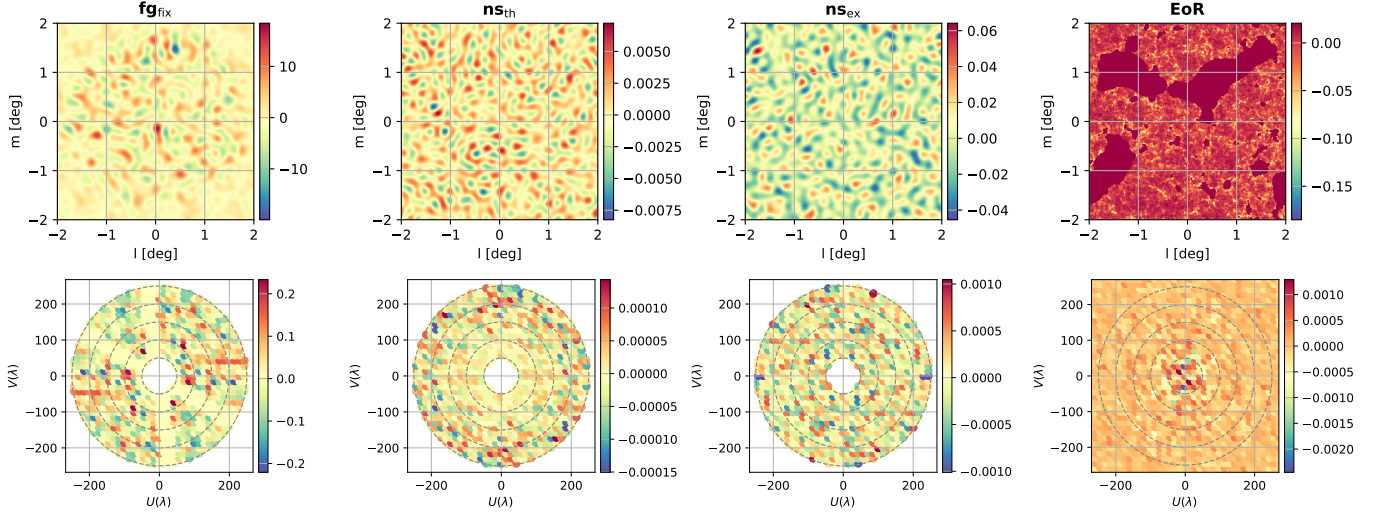


Figure 1. Simulated slices of images (first line) and visibilities (second line) from SKA before applying LOFAR uv-coverage of \mathbf{fg}_{fix} , \mathbf{ns}_{th} , \mathbf{ns}_{ex} , and \mathbf{EoR} , where \mathbf{fg}_{fix} is the smooth foreground residual obtained via GPR based on observations of the real NCP sky field; \mathbf{ns}_{th} and \mathbf{ns}_{ex} are obtained based on LOFAR’s imaging capabilities and sensitivity, respectively; and \mathbf{EoR} is obtained from full uv-coverage using **21cmFAST** code. The units of images and visibilities are both Kelvin (K).

Within this equation, σ^2 represents the variance, η denotes the functional forms of Matern class functions in special cases, Γ is the Gamma function, l represents the frequency coherence scale, $r = |\nu_p - \nu_q|$ indicates the frequency separation, and K_η refers to the modified Bessel function of the second kind.

In previous work, Gehlot et al. (2019); Mertens et al. (2020); Gehlot et al. (2020); Munshi et al. (2024a) tried to obtain the 21-cm signal using GPR and eventually provided the upper limits of the 21-cm signal. We generate the foreground residual that we need based on $\mathbf{K}_{\text{fg}}(\nu_p, \nu_q)$ in Mertens et al. (2020) which is mainly composed of intrinsic sky emission from confusion-limited extragalactic sources and from our own Galaxy $\mathbf{K}_{\text{int}}(l_{\text{int}}, \sigma_{\text{int}}^2)$ (Mertens et al. 2018), and of mode-mixing contaminants $\mathbf{K}_{\text{mix}}(l_{\text{mix}}, \sigma_{\text{mix}}^2)$ (Morales et al. 2012; Vedantham et al. 2012).

It should be noted that the datacube obtained from the observation is in the form of $64 \times 480 \times 480$ and consists of 64 frequency channels. Since deep learning requires a lot of computational resources and training time, we need to balance the Graphic Processing Unit (GPU) memory size with the complexity of the deep learning network and the size of the data set. To facilitate the deep learning process, we down-sample the resolution of the mock datacube, resulting in a $64 \times 256 \times 256$ datacube. Additionally, for a realistic simulation of the NCP field, the smooth foreground residual in this part is kept fixed. Hence, random realizations of the residuals, during training of the network, arise only from the excess variance, thermal noise, and 21-cm signals, which will be elaborated on later. This part of the foreground is referred to as \mathbf{fg}_{fix} . Since LOFAR and SKA have similar antenna place-

ment strategies, we believe that they have statistically similar behavior in their observations. Here we use the actual foreground residuals of LOFAR’s NCP sky field as the mock foreground residuals for SKA. In Fig. 1, we show a slice of the \mathbf{fg}_{fix} cube for SKA.

2.2. Thermal noise

We employ time-differential Stokes V image cubes to estimate the thermal noise. Given that thermal noise is naturally Gaussian, it can be effectively simulated using GPR. \mathbf{ns}_{th} refers to this component, whose datacube architecture mirrors that of \mathbf{fg}_{fix} .

We modeled the thermal noise on the basis of the imaging capabilities and sensitivities of LOFAR and SKA over a 1400-hour observation period. The thermal noise image and uv-coverage assumed for SKA are shown in Fig. 1 along with the other components. Since LOFAR and SKA-Low share very similar antenna array configurations, we determine their corresponding scaling factor σ_{ns}^2 and the fixed noise covariance for GPR \mathbf{K}_{ns} by utilizing LOFAR’s actual observational data, the instrument’s observational capabilities, and the observation duration. We evaluated the amplitude variance between two simulated thermal noise sky maps, as shown in Fig. 2. It is observed that the thermal noise after 1400 hours of SKA-Low observations is approximately 5% of the thermal noise present in current LOFAR observations after 141 hours of observations.

2.3. Excess variance

Mertens et al. (2020) and Munshi et al. (2024a) demonstrate that the data contain extra power on a small coherence scale, with a strength between the foreground residual

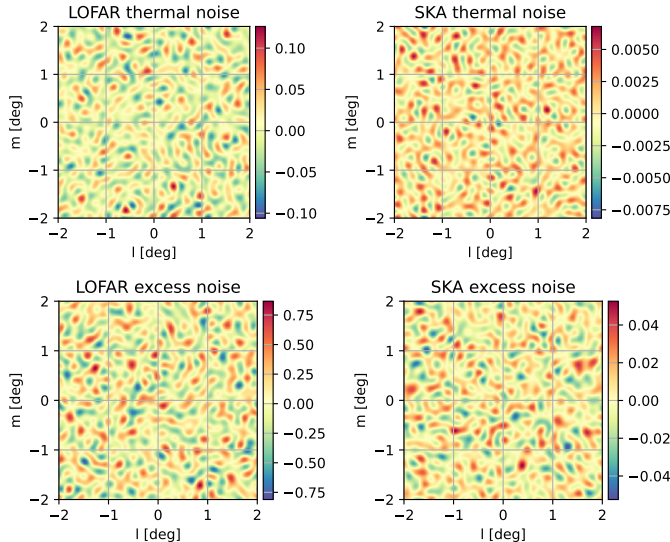


Figure 2. Thermal noise slices and excess variance slices for LOFAR and SKA, generated by GPR. The unit of images is K.

and the 21-cm signal. This additional power primarily stems from systematic errors, including instrumental effects, RFI, and suboptimal calibration. Because of the typically small-scale nature of these excess components in the residuals, it is not easy to differentiate them from the 21-cm signal. Due to the complexity of modeling these components, we continue employing GPR for excess variance simulations to generate mocks. An exponential covariance model with $\eta_{ex} = \frac{5}{2}$ is strongly favored by the observation data from LOFAR in Eq. (4) and we finally get $\mathbf{K}_{ex}(l_{ex}, \sigma_{ex}^2)$. This component is denoted as \mathbf{ns}_{ex} , and the structure of the data cube for \mathbf{ns}_{ex} is identical to that of \mathbf{fg}_{fix} . LOFAR observations reveal an excess variance with $l_{ex} = 0.26$ MHz. Furthermore, the excess variance σ_{ex}^2 is found to be 2.18 times the thermal noise variance σ_{ns}^2 . Based on these assumptions, we construct excess variance cubes for LOFAR and SKA, using the thermal noise variances discussed in the preceding subsection, as illustrated in Fig. 2, and assuming the ratio between excess variance and thermal noise is invariant. The latter is partly motivated by the fact that the excess variance appears to be largely incoherent between different observations (Mertens et al. 2020). To facilitate comparison, Fig. 1 shows the excess variance image and uv-coverage of SKA alongside the other components.

2.4. EoR signal

We generated the original 21-cm signals using the **21cmFAST** code and expanded the data set through rotations and reflections.

2.4.1. EoR data cube with full uv-coverage

For the 21-cm signal, we employ the **21cmFAST** (Mesinger et al. 2011; Murray et al. 2020) code to simulate the 21-cm brightness temperature cubes. We set the cosmological parameter S_8 to 0.8. The cube corresponds to our redshift of interest ($z \approx 9.1$) and contains a $4^\circ \times 4^\circ$ sky field with 256 pixels in each direction. In order to maintain consistency with the shape of the preceding components, we sampled the initial pixel from every quartet of pixels along the line-of-sight axis. This process generated a voxel cube of dimensions $64 \times 256 \times 256$. We denote this component by **EoR** for brevity. Fig. 1 presents a slice of the **EoR** cube and the corresponding uv-coverage in the fourth column. The uv-coverage slice of **EoR** provided by **21cmFAST** is full coverage, resulting in a more pronounced structure compared to the other components. The distribution of the **EoR** power is non-Gaussian.

2.4.2. Rotation of **EoR** data cube

Taking into account the processing speed of GPR and the anticipated volume of data sets required for subsequent deep learning applications, we ultimately generated 536 data sets. For \mathbf{fg}_{fix} , \mathbf{ns}_{ex} , and \mathbf{ns}_{th} , GPR enables a relatively rapid production of 536 data cubes.

Considering the time cost, we only used the **21cmFAST** code to generate 67 sets of brightness temperature cubes for **EoR**. Subsequently, we applied rotation and reflection operations along the line-of-sight axis to the data cube. Specifically, for each slice along this axis, we swapped the first slice with the last, the second slice with the second-to-last slice, and continued this process symmetrically until all slices were exchanged. We ended up with the above-mentioned 536 augmented data cubes for **EoR**.

2.5. Mask on uv-coverage

As shown in Fig. 1, the uv-coverage of the foreground residuals is different from the uv-coverage of the other components. For the foreground residuals, we used the same post-flagging uv-coverage as in the LOFAR observations. In addition, there is a cross-like mask in the uv-coverage due to the fact that in the LOFAR observations, we flagged side-lobe residuals of CasA and CygA that appear along nearly linear lines in uv-space (see Munshi et al. (2024b)) for a discussion of this effect), whereas for thermal noise and excess variance, the observation frequency is set to be the same as that of the foreground residuals, but the effect of a strong radio source is not taken into account. For the 21-cm signal, the uv-coverage is full between the scales corresponding to the pixel and the full image cube. Therefore, we also need to use the mask of LOFAR in the observations for the uv-coverage of thermal noise, excess variance, and 21-cm signal which are shown in Fig. 3.

By comparing Figs. 1 and 3, we find that the 21-cm signal in Fig. 3 becomes significantly more difficult to detect. This

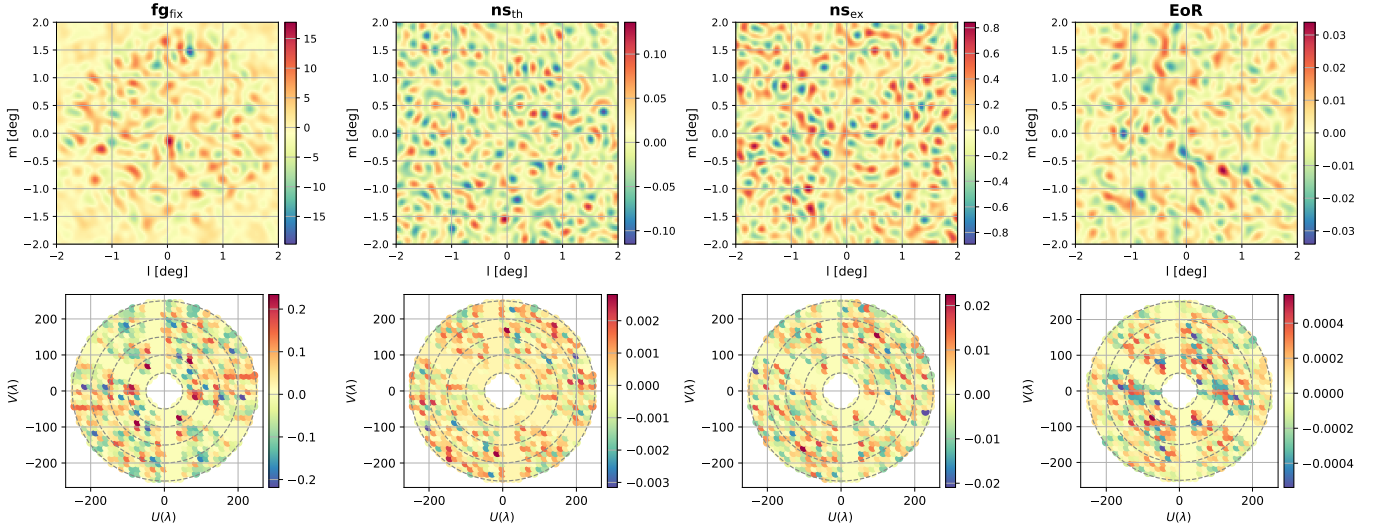


Figure 3. Simulated slices of images (first line) and visibilities (second line) from SKA after applying LOFAR uv-coverage of \mathbf{fg}_{fix} , \mathbf{ns}_{th} , \mathbf{ns}_{ex} , and \mathbf{EoR} for the slices in Fig. 1. The units of images and visibilities are both K.

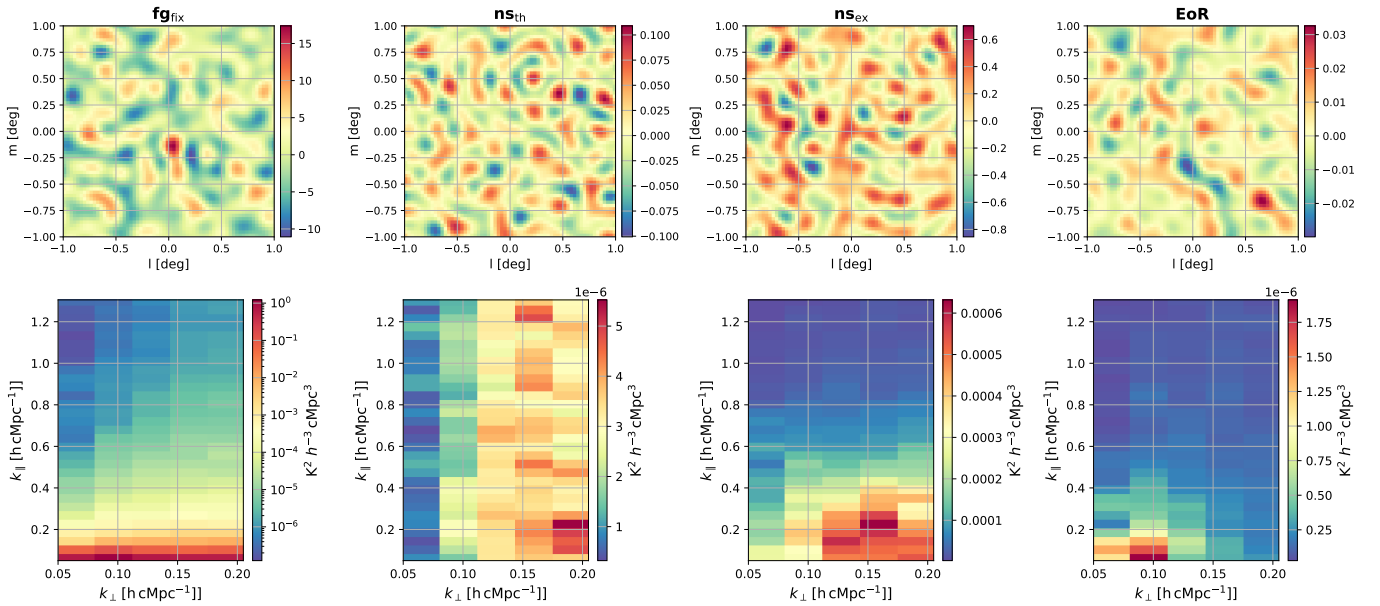


Figure 4. Slices of the middle 64×64 pixel images (first line) of the four components \mathbf{fg}_{fix} , \mathbf{ns}_{th} , \mathbf{ns}_{ex} , and \mathbf{EoR} in Fig. 3 and their corresponding 2D power spectra (second line). The units of images are both Kelvin (K). The color bar of \mathbf{fg}_{fix} 2D power spectrum is plotted using logarithmic normalization to better represent the dynamic range of the data.

is because after using the uv-coverage of LOFAR, small-scale information in the sky map is filtered out. The thermal noise and excess variance, on the other hand, do not change significantly in appearance.

Because of the imprint of the primary beam near the edges of the foreground residual, we selected the 128×128 part in the middle of each frequency channel for the subsequent study. We thus get $536 \times 64 \times 128 \times 128$ simulated data for every component, where 536 is the number of simulated data

cubes and 64 is the number of frequency channels. However, this volume of about 500 million voxels is still a challenge for subsequent deep learning in terms of GPU memory. We therefore averaged over 2×2 neighboring pixels in each frequency slice to end up with a final data set with the shape of $536 \times 64 \times 64 \times 64$. We illustrate the slices of the components and their corresponding 2D power spectra for one of the data cubes in Fig. 4.

3. SIGNAL SEPARATION VIA U-NET

This study employs a U-Net architecture, which is based on convolutional neural networks (CNNs) to attempt to separate the 21-cm signal from the noise, foregrounds, and excess variance components. Due to the large memory requirements of deep learning, we utilized an NVIDIA A100 Tensor Core GPU with 80 GB of memory in the DAWN compute cluster located at the Center for Information Technology of the University of Groningen (Pandey et al. 2020). We have 536 data sets available for deep learning. Of these, the 512 sets are designated for training, the 16 sets for validation, and the remaining 8 sets are reserved for testing.

3.1. The U-Net architecture

The U-Net network is a widely used deep learning architecture that was initially used in tasks such as image segmentation in biomedical science (Ronneberger et al. 2015). Due to its ability to generate an output data set with the same shape as the input while extracting essential features, U-Net has been widely utilized in the processing of sky maps (Gagnon-Hartman et al. 2021; Kennedy et al. 2024; Bianco et al. 2024). In prior research using the U-Net architecture as described in Makinen et al. (2021), we conducted various tests. For example, at low redshift with MeerKAT (Santos et al. 2017; Li et al. 2021; Wang et al. 2021), a precursor of SKA-Mid, we addressed beam effects (Ni et al. 2022) as well as polarization leakage (Gao et al. 2023).

The 4-layer U-Net architecture is depicted in Fig. 5. The green square on the far left represents the input data set, while the black square on the far right denotes the output data set. The U-Net architecture is divided into two primary sections: the left side of the 'U' is responsible for down-sampling, whereas the right side handles up-sampling. The convolutional network in each layer of the down-sampling processing contains 3 convolutional blocks. The first convolutional network contains 64 convolutional kernels, and the size of each convolutional kernel is $3 \times 3 \times 3$. To reduce information loss and reduce dimensionality more smoothly, we need to ensure that the stride is smaller than the length of the convolution kernel, so we set the stride = 2. Each convolutional network is followed by a rectified linear unit (ReLU) activation. Convolutional kernels and ReLU activations are represented within yellow boxes in Fig. 5. Following this, we employ a maximal set operation (red box), which can also be referred to as a pooling layer. This down-sampling process condenses the structural information of the input data cube into a reduced set of features. Since we set a growth factor of 2, each pooling operation results in a halving of the spatial dimension, and the number of channels increases by a factor of 2 of the previous layer. The parameters related to the down-sampling processing are listed in Table 1. For the up-sampling process, the blue part repre-

sents the transposed convolution and the gray sphere denotes the connected layer. The transposed convolution operation is capable of expanding the spatial dimensions of a feature map from a lower resolution to a higher resolution. The connected layer links the corresponding layers involved in both down-sampling and up-sampling processes, thereby preventing information loss that can occur with increasing network depth and aiding in the retention of small-scale image structures. Throughout the entire learning process, we employ the AdamW optimizer (Loshchilov & Hutter 2017) to achieve a stepwise reduction in the learning rate.

3.2. Loss function

The loss function in deep learning quantifies the disparity between the predicted values generated by a network and the actual true values. The standard Mean Square Error (MSE) loss function is the most frequently utilized; however, it exhibits substantial instability when processing images. Consequently, we employ the more stable Log-Cosh loss function, which enhances the management of outlier points. The Log-Cosh loss function is defined as

$$\mathcal{L} = \sum_i \log \cosh(p_i - t_i), \quad (5)$$

where p_i represents the predicted outcome and t_i corresponds to the actual signal of the i -th voxel, respectively. We also considered calculating the loss in uv-coverage instead of image space. But since there is no obvious relationship between neighboring pixels in uv-coverage, the results obtained are significantly worse than operating in image space.

3.3. Hyperparameter selection

Hyperparameters determine key aspects of network architecture, learning process, optimization methods, and regularization strategies. We list the hyperparameters used by U-Net in Table 1. We have already described the setting of the hyperparameters related to the convolutional and pooling layers of the deep learning network used in Section 3.1. We configure n_{down} to 4 to allow the network to access all data. Since the 21-cm signal is extremely weak, our primary focus is on utilizing the most fine-tuned neural network that the GPU memory capacity can support, rather than optimizing for speed. Setting n_{block} to 3 ensures that we get more information about the features and prevents loss of information. To facilitate the use of complex neural network structures, we maintain a relatively modest common batch size of 16. We utilize 64 initial convolution filters per block to thoroughly capture detailed features. We use a smaller learning rate ($\eta = 10^{-5}$) to mitigate overfitting, complemented by the AdamW optimizer (Loshchilov & Hutter 2017), which adjusts the learning rate during training to further prevent overfitting. The weight decay ω in the optimizer is set to 10^{-5} . We also

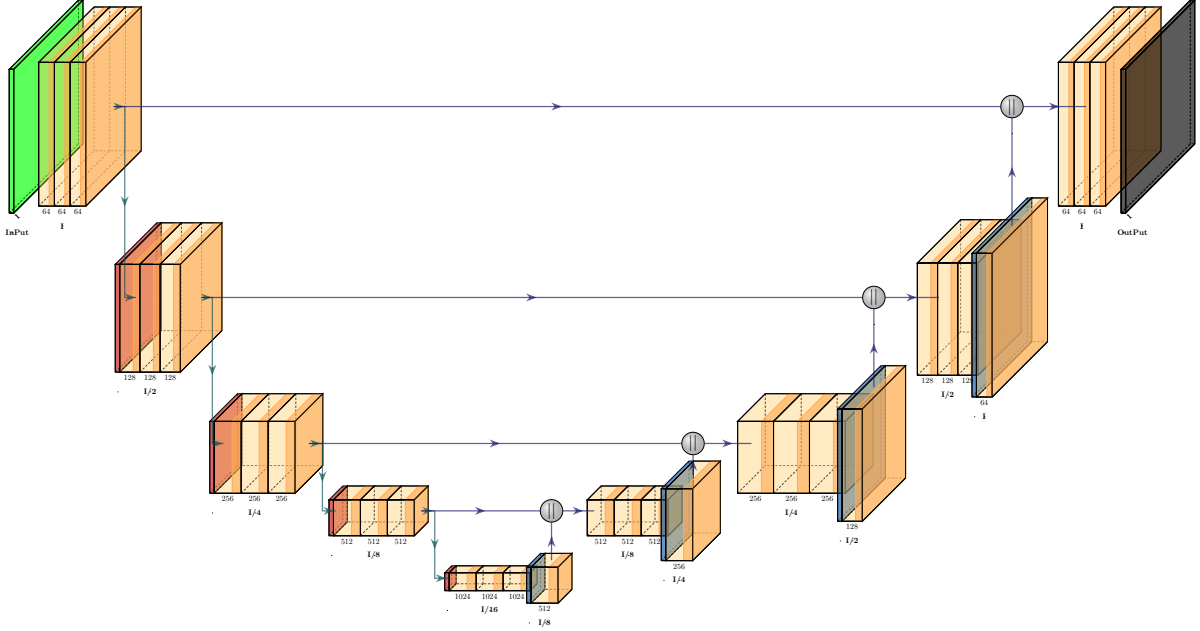


Figure 5. Training process of CNNs with U-Net architecture. Each color represents a structure in the U-Net network, where yellow cubes represent the convolutional layers and ReLU sections, red cubes represent pooling layers in down-sampling, blue cubes represent the transposed convolutional layers, and gray spheres represent connection layers. The green and black squares at the beginning and end of this figure represent the input and output, respectively.

Table 1. Description of the hyperparameters in the U-Net architecture design.

Hyperparameter	Value
convolution width (number of convolutions in each layer)	3
kernel size (size of the convolution kernel)	$3 \times 3 \times 3$
growth factor (Growth rate of channels in each layer)	2
stride (step size of each move of the convolution kernel)	2
n_{block} (number of convolutions for each block)	3
n_{down} (number of down-convolutions)	4
batch size (number of samples per gradient descent step)	16
n_{filter} (initial number of convolution filters)	64
η (learning rate for optimizer)	10^{-5}
Ω (optimizer for training)	AdamW
ω (weight decay for optimizer)	10^{-5}
β_{mom} (batch normalization momentum)	0.02

set the batch normalization momentum (β_{mom}) to 0.02 to enhance the stability of the neural network.

4. RESULTS AND DISCUSSION

In this section, we examine the ability of 3D U-Net to extract the 21-cm signal based on different components and observation times of the mock SKA data. Furthermore, we conduct a robustness analysis to assess to what level the 3D U-Net can recover the 21-cm signal in the foreground-wedge region.

4.1. Signal extraction from $\text{ns}_{\text{th}} + \text{EoR}$

Based on 1400 hours of SKA-Low observations, both fg_{fix} and ns_{ex} far exceed the 21-cm signal, while ns_{th} is an order of magnitude below the 21-cm signal on most baselines simulated in this work. As a first step, we evaluate a simplified scenario, focusing solely on the 21-cm signal and ns_{th} , while disregarding fg_{fix} and ns_{ex} .

We find that the 3D U-Net can easily extract the required information, since the thermal noise level is small relative to the 21-cm signal, allowing U-Net to discern finer structures. Consequently, we require more training epochs to achieve optimal results. After 2500 epochs, the loss-function value of the U-Net stabilizes, and further training did not result in overfitting. It is important to note that varying data combinations, each with unique structures and errors, require different numbers of training epochs to maintain stability and prevent overfitting, as will be demonstrated next. The target 21-cm signal image and the U-Net output are illustrated in Fig. 6 for a typical case. Although there are some small differences, U-Net recovers most structures successfully. This conclusion is supported by the 2D cross power spectrum and 2D coherence power spectrum between the target **EoR** and U-Net images, as shown in Fig. 7. We see that the coherence is very close to unity and only for a higher k-mode decreases a little due to the thermal noise.

4.1.1. Robustness analysis

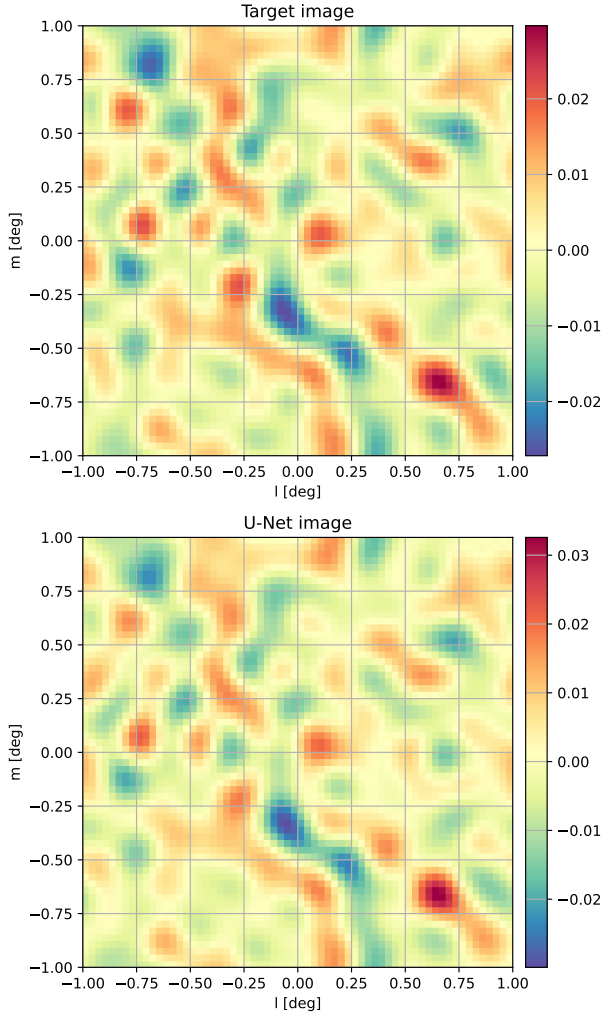


Figure 6. Target EoR image and predictive images given by U-Net when considering only the effects of ns_{th} . These images are in units of K.

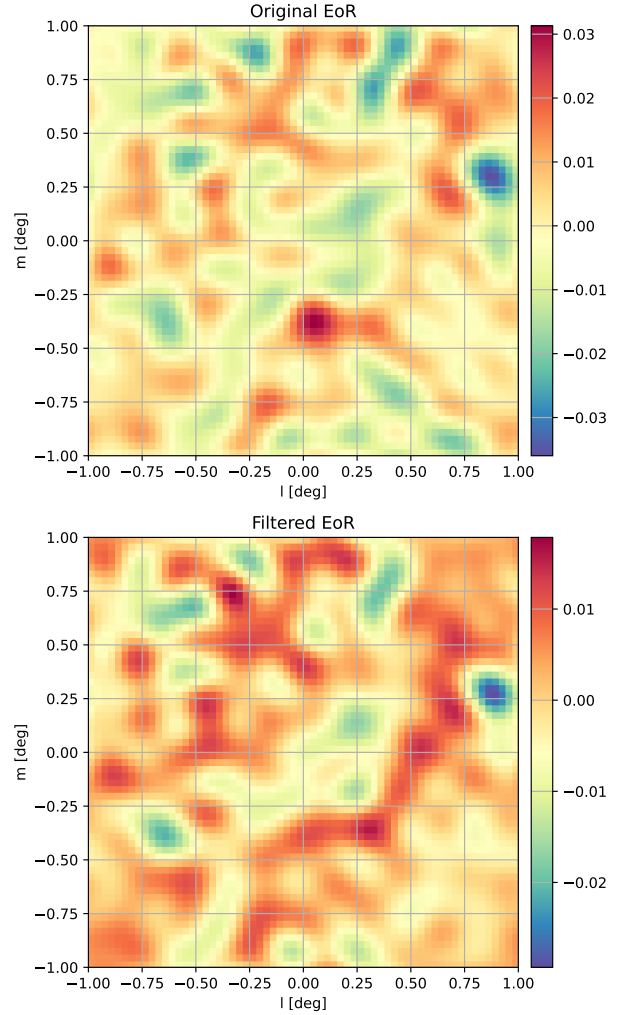


Figure 8. Original EoR_{ori} image and regenerated EoR_{rev} image by removing the 30° filter wedge in the 2D power spectrum. These images are in units of K.

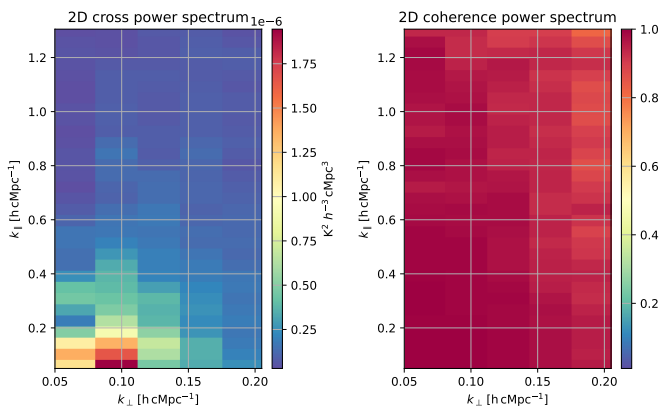


Figure 7. 2D cross power spectrum and 2D coherence power spectrum between the target EoR and U-Net predictive image when considering only the effects of ns_{th} .

In the following subsections, we will assess the impact of the foregrounds (fg_{fix}) and the excess variance (ns_{ex}) on the recovery of the 21-cm signal using U-Net, showing that recovery becomes more difficult. However, U-Nets are also capable of predicting signals in regions where they are not measured (e.g., inside the wedge) using nearby information (e.g. outside the wedge). We therefore first need to assess whether our U-Net predicts or genuinely recovers the 21-cm signal inside the wedge region.

To confirm this, we used a filter wedge with a 30° angle. For EoR, the part of the power spectrum within the filter wedge is excluded, resulting in a revised EoR sky map. To distinguish them, we call them EoR_{ori} and EoR_{rev} respectively. We present both the EoR_{ori} image and the EoR_{rev} image obtained after removing the filter wedge from the 2D power spectrum in Fig. 8. Furthermore, Fig. 9 presents their respective 2D power spectra along with their 2D coherence

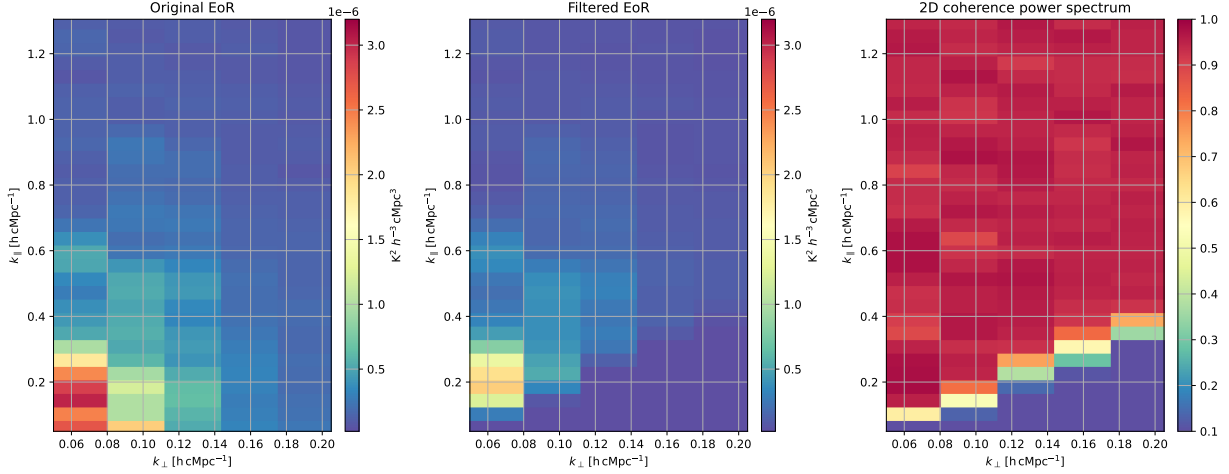


Figure 9. Original $\mathbf{EoR}_{\text{ori}}$ 2D power spectrum, $\mathbf{EoR}_{\text{rev}}$ 2D power spectrum after removing the 30° filter wedge, and their 2D coherence power spectrum between them. We find that these two spectra are different in scale before and after filtering. Due to windowing effects based on the finite frequency bandwidth of the observations, it leads to some leakage from scales below the wedge to above the wedge after, and visa versa. Hence, removing modes below the wedge leads to a minor change in both power and coherence above the wedge as well.

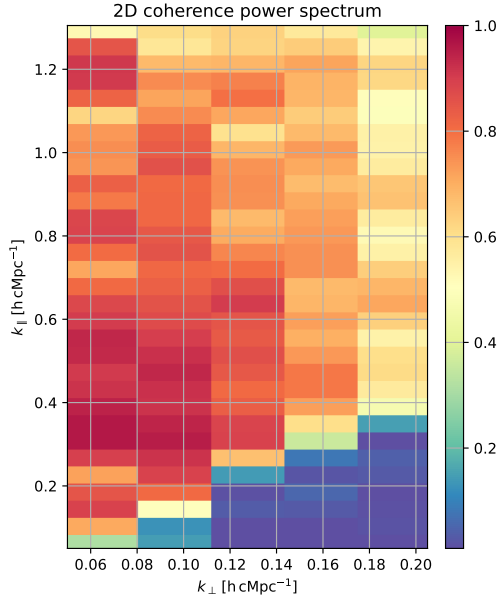


Figure 10. 2D coherence power spectrum of U-Net predicted $\mathbf{EoR}_{\text{rev}}$ image and target $\mathbf{EoR}_{\text{ori}}$ image.

power spectrum. As demonstrated in Fig. 8, the peak intensity of the $\mathbf{EoR}_{\text{rev}}$ decreases considerably with the removal of the wedge, but they remain very similar in their overall structure.

We utilized the original \mathbf{ns}_{th} image combined with the $\mathbf{EoR}_{\text{rev}}$ image as the input, with the $\mathbf{EoR}_{\text{ori}}$ image serving as the target, and fed them into the 3D U-Net model. After 700 epochs of training, the coherence 2D power spectrum between the U-Net predicted skymap and the target skymap was obtained as shown in Fig. 10. Continuing the training process will result in the neural network becoming over-fitted to the

training data set. By analyzing the coherence power spectra in Figs. 9 and 10, we conclude that the neural network does not predict the filtered-out part, i.e., in the wedge, of the power spectrum. Consequently, we conclude that any recovered 21-cm signal below the wedge in the presence of strong foreground and excess variance, as presented in the following sub-sections, is not due to a prediction from signal above the wedge, but a genuine signal recovery.

4.2. Signal extraction from $\mathbf{fg}_{\text{fix}} + \mathbf{ns}_{\text{th}} + \mathbf{EoR}$

Here we examine the influence of the fixed foreground residual \mathbf{fg}_{fix} and thermal noise \mathbf{ns}_{th} , on the signal extraction. Given that the foreground remains fully coherent during the observation period, it is primarily excess variance and thermal noise that impact the observations during training, and the foreground residuals are based on the foreground residuals (after sky-model subtraction) from LOFAR observations. Therefore, we treat the foreground residual as fixed. In order to further evaluate the U-Net's capability to extract the \mathbf{EoR} signal, for now, we assume ideal observations without any systematic effects such as the excess variance due to mode mixing. It should be noted that in this training process, the input consists of $\mathbf{fg}_{\text{fix}} + \mathbf{ns}_{\text{th}} + \mathbf{EoR}$.

Fig. 11 shows the 2D cross power spectrum and 2D coherence power spectrum between the target \mathbf{EoR} image and the U-Net predicted image from 2000-epoch training after including the fixed foreground model. Comparing Fig. 7 and Fig. 11 above the horizon, we see that both give excellent 21-cm signal recovery over much of the probed spatial scales. It shows that for small-scale structures, the fixed foreground residuals do not affect the training results. However, for a small section below the horizon, there is a more pronounced inconsistency in its lower right corner in Fig. 11, which is

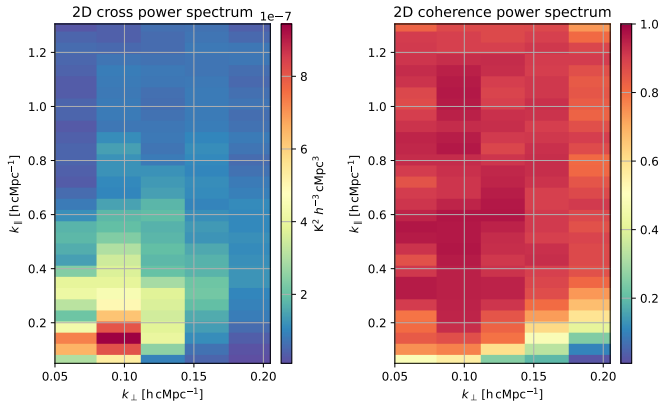


Figure 11. 2D cross power spectrum and 2D coherence power spectrum between the target **EoR** and U-Net predictive image when considering the effects of \mathbf{fg}_{fix} and \mathbf{ns}_{th} .

consistent with the signal extraction results from other methods. Examining the power spectrum of the foreground residual illustrated in Fig. 4 alongside the 2D coherence power spectrum in Fig. 11 reveals that U-Net is unable to accurately reproduce the power spectrum in areas where the intensity of the foreground residuals is high, despite the fixation of the foreground residuals we included in the analysis. To solve this problem, we will examine a combination of using GPR and U-Nets in a future publication since the GPR in general is quite effective in removing those modes from the data, and this seems to be necessary for the U-net to perform optimally.

4.3. Signal extraction from $\mathbf{ns}_{\text{ex}} + \mathbf{ns}_{\text{th}} + \mathbf{EoR}$ with different observation time

Here we have considered the effect of the excess variance (\mathbf{ns}_{ex}) in addition to the thermal noise (\mathbf{ns}_{th}). Since the effect of \mathbf{fg}_{fix} on the extraction of the 21-cm signal is mainly in the small k_{\parallel} region and can probably be removed using GPR, we decided to ignore the effect of \mathbf{fg}_{fix} to prevent over-stressing U-Net processing. Note that the \mathbf{ns}_{ex} we use here is a Gaussian random field, but in real observations, the \mathbf{ns}_{ex} could have some correlated structures. Since Gaussian \mathbf{ns}_{ex} makes the distribution of the intensities uncorrelated in phase space, we believe that in real observations better results could be obtained.

To determine at what noise level U-Net remains effective, we varied the duration of the observation. Initially, we examined a 1400-hour observation for consistency with the previous analysis, followed by observations of 3700 hours and an extreme case of 14000 hours. For convenience, we refer to the sum of \mathbf{ns}_{ex} and \mathbf{ns}_{th} as \mathbf{ns}_{all} . As the observation time increases, the excess variance decreases. For example, the intensity at 3700 hours of \mathbf{ns}_{all} is about half that of 1400 hours of \mathbf{ns}_{all} , and at 14000 hours, the intensity is approximately 70% of what it is at 3700 hours of \mathbf{ns}_{all} . In Fig. 12, we illustrate some of the \mathbf{ns}_{all} images obtained with different ob-

servations. Observations over 1400 hours show a peak amplitude of approximately 0.04K, while those over 3700 hours exhibit an amplitude close to 0.025K. For the 14000-hour observations, the maximum amplitude is about 0.015K, in all cases dominated by the excess variance component. We note that the variation in the level of thermal and excess noise influences the required number of epochs to achieve stability in U-Net training. Increasing the number of epochs, however, can result in overfitting. This occurs because weaker structures are overwhelmed by Gaussian random field errors \mathbf{ns}_{all} , and when U-Net tries to capture the structure after noise saturation, it results in larger errors. Observations lasting 1400 hours require 600 epochs for U-Net, while 3700 hours of observations require 1000 epochs, and a total of 14000 hours of observations require 1400 epochs.

In Fig. 13, we show the 2D cross power spectra and 2D coherence power spectra of the predicted and target **EoR** images obtained via U-Net based on images at different observation times, respectively. Our results indicate that across different observations, better outcomes are typically observed at higher k_{\parallel} and lower k_{\perp} , as expected, since the impacts of the thermal noise and excess variance are smaller in those regions. Notably, for 1400 hours of observation, there is a marked alteration in the 2D coherence power spectrum when k_{\perp} equals 0.113. This shift may be attributed to the rapidly increasing dominance of the \mathbf{ns}_{all} intensity over the **EoR** signal, leading to the masking of fine details in the 21-cm signal by Gaussian errors, restricting the U-Net to mainly capture larger-scale information. In the case of 3700 hours of observation, the delimitation on k_{\perp} becomes less distinct; however, the 2D coherence power spectrum still exhibits inconsistencies below the horizon, similar to those in real observations. Meanwhile, improvements are noted for signals above the horizon. Finally, after 14000 hours of observations, the intensity of \mathbf{ns}_{all} is roughly half that of the **EoR** signal, allowing for a reliable **EoR** 2D cross power spectrum even below the horizon. We note, however, that obtaining 14000 hours of observations with SKA-Low on deep fields is not a likely scenario and a more effective way to recover the signal with shorter integration times would be to more effectively reduce excess variance, which we assumed here to be the same between LOFAR and SKA-Low, be incoherent, and scale down with thermal noise in the same way. It is very likely, however, that SKA-Low will have less excess variance due to its better beam control and better instantaneous uv-coverage, leading to lower gain errors.

5. SUMMARY AND CONCLUSION

Extracting the **EoR** signal from observations presents significant challenges due to inhomogeneous and spectrally varying uv-coverage, bright foreground emission, thermal noise, and various systematic effects such as beam errors.

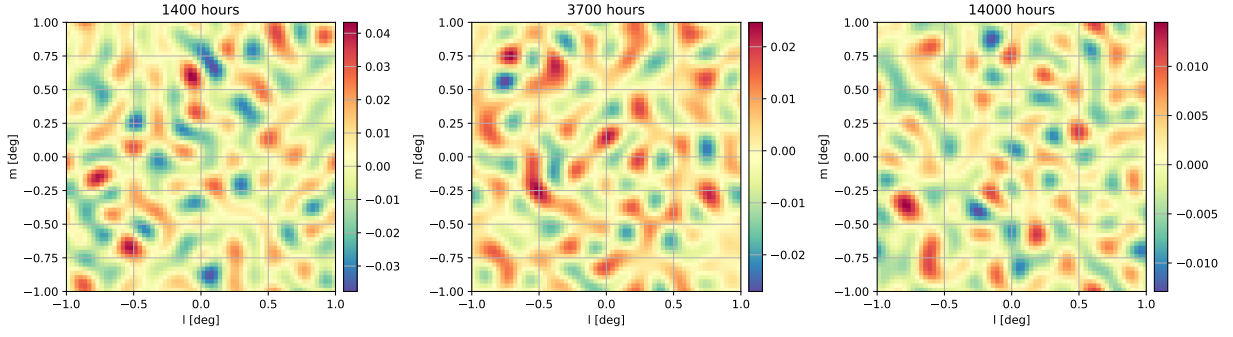


Figure 12. Images of the ns_{all} at observation times 1400 hours, 3700 hours and 14000 hours, respectively. These images are in units of K.

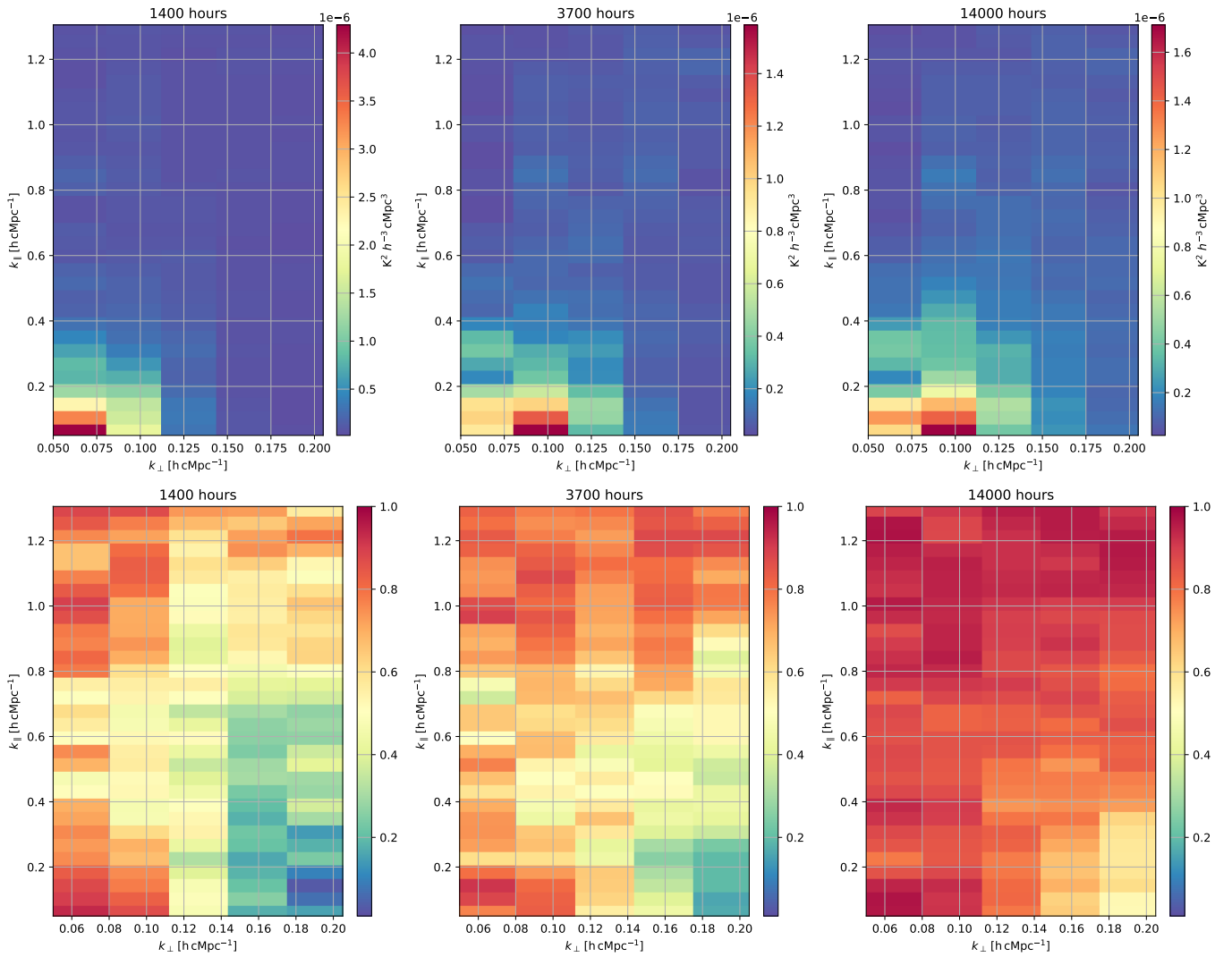


Figure 13. The 2D cross power spectra (first row) and their corresponding 2D coherence power spectra (second row) of predicted and target images derived from U-Net processing of simulated data, which was observed for durations of 1400 hours, 3700 hours, and 14000 hours.

This paper examines SKA-Low-like observations, focusing on thermal noise and different systematic effects predominantly excess variance. We assumed a similar uv-coverage as for LOFAR and restricted the analysis to the 50 – 250 λ baseline range, including the current flagging mask of LOFAR EoR observations. We concentrate on SKA-Low results, as LOFAR’s noise levels are currently too high, whereas SKA’s expected noise is approximately 5% of LOFAR’s current noise level.

We used foreground residuals from actual observations of the NCP field, excess power and thermal noise based on GPR, along with EoR signals produced by **21cmFAST**.

We employed a 3D U-Net neural network for analyzing various sky maps. Initially, we evaluated a basic scenario that considered only the ns_{th} and EoR signals. Over 1400 hours of observation, the SKA’s ns_{th} level is below that of the EoR signal, enabling U-Net to reliably produce a 2D power spectrum for EoR. We also examined the robustness of our results, showing that the 21-cm signal recovered in the wedge regions is not due to U-Net predictions from signals above the wedge. The 30° filter wedge was removed from the 2D power spectra of the EoR_{ori} signal, and the EoR_{rev} images were regenerated based on that. We also investigated the impact of foreground residuals alongside previous findings, which revealed a significant discrepancy in the lower right of the 2D coherence power spectrum. This is consistent with the processing of real observations and is due to the dominance of the foreground in the large-scale structure of the line-of-sight direction. Lastly, the joint influence of both ns_{th} and ns_{ex} on the EoR signal extraction were examined. Given that ns_{ex} exceeds the intensity of the EoR signal only after about 1400 hours, we approached the results with caution. Thus, observations were also extended to 3700 and 14000 hours. At 1400 hours, parts of the 2D coherence power spectrum above the horizon show weaker correlations, but regions with k_{\perp} values below 0.113 produced reliable results. For 3700 hours, reliable results were achieved within the entire EoR window. With 14000 hours, consistent 2D coherence power spectra were observed both above and below the horizon set by the excess variance. This

suggests a promising future role for the 3D U-Net neural network in processing real SKA observational data, but that any presence of residual foreground and excess variance, as observed in current LOFAR data, could have a significant impact on the recovery of the 21-cm signal below the horizon delay line. These contaminations cannot be easily removed even with deep learning techniques and the most effective way forward is to reduce these contaminations by improving data calibrations and foreground subtraction methods as discussed by Acharya et al. (2024).

ACKNOWLEDGEMENTS

We are grateful for the support of the National SKA Program of China (Grants Nos. 2022SKA0110200 and 2022SKA0110203), the National Natural Science Foundation of China (Grant Nos. 12473001, 11975072, and 11875102), the Liaoning Revitalization Talents Program (Grant No. XLYC1905011), the 111 Project (Grant No. B16009), the Top-Notch Young Talents Program of China (Grant No. W02070050), the China Manned Space Project (Grant NO.CMS-CSST-2021-B01), the European Research Council (ERC) under the European Union’s Horizon 2020 research and innovation programme (Grant agreement No. 884760, ”CoDEX”), Science and Engineering Research Board - Department of Science and Technology (SERB-DST) Ramanujan Fellowship (Grant agreement NO. RJF/2022/000141) the European Research Council (ERC) under the European Union’s Horizon 2020 research and innovation programme (Grant agreement No. 884760, ”CoDEX”), Science and Engineering Research Board - Department of Science and Technology (SERB-DST) Ramanujan Fellowship (Grant agreement NO. RJF/2022/000141), the Centre for Data Science and Systems Complexity (DSSC), Faculty of Science and Engineering at the University of Groningen, the Swedish Research Council (Grant agreement No. 2020-04691), and the Ministry of Universities and Research (MUR) through the PRIN project ‘Optimal inference from radio images of the epoch of reionization’.

REFERENCES

- Acharya, A., Mertens, F., Ciardi, B., et al. 2024, *Mon. Not. Roy. Astron. Soc.*, 534, L30, doi: [10.1093/mnras/slaf078](https://doi.org/10.1093/mnras/slaf078)
- Ananthakrishnan, S. 1995, *Journal of Astrophysics and Astronomy*, 16, 427
- Ansari, R., Campagne, J. E., Colom, P., et al. 2012, *Astron. Astrophys.*, 540, A129, doi: [10.1051/0004-6361/201117837](https://doi.org/10.1051/0004-6361/201117837)
- Asad, K. M. B., Koopmans, L. V. E., Jelić, V., et al. 2018, *Monthly Notices of the Royal Astronomical Society*, 476, 3051, doi: [10.1093/mnras/sty258](https://doi.org/10.1093/mnras/sty258)
- Asad, K. M. B., et al. 2015, *Mon. Not. Roy. Astron. Soc.*, 451, 3709, doi: [10.1093/mnras/stv1107](https://doi.org/10.1093/mnras/stv1107)
- Asad, K. M. B., Koopmans, L. V. E., Jelić, V., et al. 2016, *Monthly Notices of the Royal Astronomical Society*, 462, 4482, doi: [10.1093/mnras/stw1863](https://doi.org/10.1093/mnras/stw1863)
- Barry, N., Bernardi, G., Greig, B., Kern, N., & Mertens, F. 2021, *J. Astron. Telesc. Instrum. Syst.*, 8, 011007, doi: [10.1117/1.JATIS.8.1.011007](https://doi.org/10.1117/1.JATIS.8.1.011007)

- Barry, N., et al. 2019, *Astrophys. J.*, doi: [10.3847/1538-4357/ab40a8](https://doi.org/10.3847/1538-4357/ab40a8)
- Bhatnagar, S., & Nityananda, R. 2001, *Astron. Astrophys.*, 375, 344, doi: [10.1051/0004-6361:20010799](https://doi.org/10.1051/0004-6361:20010799)
- Bianco, M., Giri, S. K., Iliiev, I. T., & Mellema, G. 2021, *MNRAS*, 505, 3982, doi: [10.1093/mnras/stab1518](https://doi.org/10.1093/mnras/stab1518)
- Bianco, M., Giri, S. K., Prelogović, D., et al. 2024a, *MNRAS*, 528, 5212, doi: [10.1093/mnras/stae257](https://doi.org/10.1093/mnras/stae257)
- Bianco, M., Giri, S. K., Sharma, R., et al. 2024b, arXiv e-prints, arXiv:2408.16814, doi: [10.48550/arXiv.2408.16814](https://doi.org/10.48550/arXiv.2408.16814)
- Bianco, M., Giri, S. K., Sharma, R., et al. 2024, <https://arxiv.org/abs/2408.16814>
- Bobin, J., Starck, J.-L., Fadili, J., & Moudden, Y. 2007, *IEEE Transactions on Image Processing*, 16, 2662, doi: [10.1109/TIP.2007.906256](https://doi.org/10.1109/TIP.2007.906256)
- Bowman, J. D., Morales, M. F., & Hewitt, J. N. 2009, *ApJ*, 695, 183, doi: [10.1088/0004-637X/695/1/183](https://doi.org/10.1088/0004-637X/695/1/183)
- Chapman, E., Abdalla, F. B., Harker, G., et al. 2012, *MNRAS*, 423, 2518, doi: [10.1111/j.1365-2966.2012.21065.x](https://doi.org/10.1111/j.1365-2966.2012.21065.x)
- Chapman, E., Abdalla, F. B., Harker, G., et al. 2012, *Mon. Not. Roy. Astron. Soc.*, 423, 2518, doi: [10.1111/j.1365-2966.2012.21065.x](https://doi.org/10.1111/j.1365-2966.2012.21065.x)
- Chen, T., Bianco, M., Tolley, E., et al. 2024, *MNRAS*, 532, 2615, doi: [10.1093/mnras/stae1676](https://doi.org/10.1093/mnras/stae1676)
- Cunnington, S., Irfan, M. O., Carucci, I. P., Pourtsidou, A., & Bobin, J. 2021, *MNRAS*, 504, 208, doi: [10.1093/mnras/stab856](https://doi.org/10.1093/mnras/stab856)
- Cunnington, S., Wolz, L., Pourtsidou, A., & Bacon, D. 2019, *Mon. Not. Roy. Astron. Soc.*, 488, 5452, doi: [10.1093/mnras/stz1916](https://doi.org/10.1093/mnras/stz1916)
- DeBoer, D. R., et al. 2017, *Publ. Astron. Soc. Pac.*, 129, 045001, doi: [10.1088/1538-3873/129/974/045001](https://doi.org/10.1088/1538-3873/129/974/045001)
- Eastwood, M. W., et al. 2019, *Astron. J.*, 158, 84, doi: [10.3847/1538-3881/ab2629](https://doi.org/10.3847/1538-3881/ab2629)
- Furlanetto, S., Oh, S. P., & Briggs, F. 2006, *Phys. Rept.*, 433, 181, doi: [10.1016/j.physrep.2006.08.002](https://doi.org/10.1016/j.physrep.2006.08.002)
- Gagnon-Hartman, S., Cui, Y., Liu, A., Ravanbakhsh, S., & Kennedy, J. 2021, *Mon. Not. Roy. Astron. Soc.*, 504, 4716, doi: [10.1093/mnras/stab1158](https://doi.org/10.1093/mnras/stab1158)
- Gao, L.-Y., Li, Y., Ni, S., & Zhang, X. 2023, *Mon. Not. Roy. Astron. Soc.*, 525, 5278, doi: [10.1093/mnras/stad2646](https://doi.org/10.1093/mnras/stad2646)
- Garsden, H., Greenhill, L., Bernardi, G., et al. 2021, *Mon. Not. Roy. Astron. Soc.*, 506, 5802, doi: [10.1093/mnras/stab1671](https://doi.org/10.1093/mnras/stab1671)
- Gehlot, B. K., Mertens, F. G., Koopmans, L. V. E., et al. 2019, *Monthly Notices of the Royal Astronomical Society*, 488, 4271, doi: [10.1093/mnras/stz1937](https://doi.org/10.1093/mnras/stz1937)
- Gehlot, B. K., et al. 2020, *Mon. Not. Roy. Astron. Soc.*, 499, 4158, doi: [10.1093/mnras/staa3093](https://doi.org/10.1093/mnras/staa3093)
- Gelman, A., Carlin, J. B., Stern, H. S., et al. 2013, *Bayesian data analysis, third edition edn.* (Chapman and Hall/CRC), doi: [10.1201/b16018](https://doi.org/10.1201/b16018)
- Hyvarinen, A. 1999, *IEEE Transactions on Neural Networks*, 10, 626, doi: [10.1109/72.761722](https://doi.org/10.1109/72.761722)
- Kennedy, J., Carr, J. C., Gagnon-Hartman, S., et al. 2024, *Mon. Not. Roy. Astron. Soc.*, 529, 3684, doi: [10.1093/mnras/stae760](https://doi.org/10.1093/mnras/stae760)
- Koopmans, L. V. E., et al. 2015, *PoS, AASKA14*, 001, doi: [10.22323/1.215.0001](https://doi.org/10.22323/1.215.0001)
- Li, W., et al. 2019, *Astrophys. J.*, 887, 141, doi: [10.3847/1538-4357/ab55e4](https://doi.org/10.3847/1538-4357/ab55e4)
- Li, Y., Santos, M. G., Grainge, K., Harper, S., & Wang, J. 2021, *MNRAS*, 501, 4344, doi: [10.1093/mnras/staa3856](https://doi.org/10.1093/mnras/staa3856)
- Loshchilov, I., & Hutter, F. 2017. <https://arxiv.org/abs/1711.05101>
- Madau, P., Meiksin, A., & Rees, M. J. 1997, *The Astrophysical Journal*, 475, 429, doi: [10.1086/303549](https://doi.org/10.1086/303549)
- Makinen, T. L., Lancaster, L., Villaescusa-Navarro, F., et al. 2021, *JCAP*, 04, 081, doi: [10.1088/1475-7516/2021/04/081](https://doi.org/10.1088/1475-7516/2021/04/081)
- Masui, K. W., et al. 2013, *Astrophys. J. Lett.*, 763, L20, doi: [10.1088/2041-8205/763/1/L20](https://doi.org/10.1088/2041-8205/763/1/L20)
- Matshawule, S. D., Spinelli, M., Santos, M. G., & Ngobese, S. 2021a, *Monthly Notices of the Royal Astronomical Society*, 506, 5075, doi: [10.1093/mnras/stab1688](https://doi.org/10.1093/mnras/stab1688)
- . 2021b, *Mon. Not. Roy. Astron. Soc.*, 506, 5075, doi: [10.1093/mnras/stab1688](https://doi.org/10.1093/mnras/stab1688)
- Mertens, F. G., Ghosh, A., & Koopmans, L. V. E. 2018, *Mon. Not. Roy. Astron. Soc.*, 478, 3640, doi: [10.1093/mnras/sty1207](https://doi.org/10.1093/mnras/sty1207)
- Mertens, F. G., et al. 2020, *Mon. Not. Roy. Astron. Soc.*, 493, 1662, doi: [10.1093/mnras/staa327](https://doi.org/10.1093/mnras/staa327)
- Mesinger, A., Furlanetto, S., & Cen, R. 2011, *Monthly Notices of the Royal Astronomical Society*, 411, 955, doi: [10.1111/j.1365-2966.2010.17731.x](https://doi.org/10.1111/j.1365-2966.2010.17731.x)
- Morales, M. F., Hazelton, B., Sullivan, I., & Beardsley, A. 2012, *Astrophys. J.*, 752, 137, doi: [10.1088/0004-637X/752/2/137](https://doi.org/10.1088/0004-637X/752/2/137)
- Munshi, S., et al. 2024a, *Astron. Astrophys.*, 681, A62, doi: [10.1051/0004-6361/202348329](https://doi.org/10.1051/0004-6361/202348329)
- Munshi, S., Mertens, F., Koopmans, L., et al. 2024b, arXiv preprint arXiv:2407.10686
- Murray, S. G., Greig, B., Mesinger, A., et al. 2020, *J. Open Source Softw.*, 5, 2582, doi: [10.21105/joss.02582](https://doi.org/10.21105/joss.02582)
- Ni, S., Li, Y., Gao, L.-Y., & Zhang, X. 2022, *Astrophys. J.*, 934, 83, doi: [10.3847/1538-4357/ac7a34](https://doi.org/10.3847/1538-4357/ac7a34)
- Nunhokee, C. D., Bernardi, G., Kohn, S. A., et al. 2017, *Astrophys. J.*, 848, 47, doi: [10.3847/1538-4357/aa8b73](https://doi.org/10.3847/1538-4357/aa8b73)
- Paciga, G., et al. 2013, *Mon. Not. Roy. Astron. Soc.*, 433, 639, doi: [10.1093/mnras/stt753](https://doi.org/10.1093/mnras/stt753)
- Pandey, V. N., Koopmans, L. V. E., Tiesinga, E., Albers, W., & Koers, H. U. A. 2020, in *Astronomical Society of the Pacific Conference Series*, Vol. 527, *Astronomical Data Analysis Software and Systems XXIX*, ed. R. Pizzo, E. R. Deul, J. D. Mol, J. de Plaa, & H. Verkouter, 473
- Patil, A. H., et al. 2017, *Astrophys. J.*, 838, 65, doi: [10.3847/1538-4357/aa63e7](https://doi.org/10.3847/1538-4357/aa63e7)

- Pritchard, J. R., & Furlanetto, S. R. 2007, *Mon. Not. Roy. Astron. Soc.*, 376, 1680, doi: [10.1111/j.1365-2966.2007.11519.x](https://doi.org/10.1111/j.1365-2966.2007.11519.x)
- Pritchard, J. R., & Loeb, A. 2012, *Reports on Progress in Physics*, 75, 086901, doi: [10.1088/0034-4885/75/8/086901](https://doi.org/10.1088/0034-4885/75/8/086901)
- Rasmussen, C. E., & Williams, C. K. I. 2005, *Gaussian Processes for Machine Learning* (The MIT Press), doi: [10.7551/mitpress/3206.001.0001](https://doi.org/10.7551/mitpress/3206.001.0001)
- Ronneberger, O., Fischer, P., & Brox, T. 2015, in *Medical image computing and computer-assisted intervention—MICCAI 2015: 18th international conference, Munich, Germany, October 5-9, 2015, proceedings, part III 18*, Springer, 234–241
- Santos, M. G., et al. 2017, in *MeerKAT Science: On the Pathway to the SKA*. <https://arxiv.org/abs/1709.06099>
- Shaver, P. A., Windhorst, R. A., Madau, P., & de Bruyn, A. G. 1999, *Astron. Astrophys.*, 345, 380. <https://arxiv.org/abs/astro-ph/9901320>
- Spinelli, M., Carucci, I. P., Cunnington, S., et al. 2021, *Mon. Not. Roy. Astron. Soc.*, 509, 2048, doi: [10.1093/mnras/stab3064](https://doi.org/10.1093/mnras/stab3064)
- Trott, C. M., et al. 2020, *Mon. Not. Roy. Astron. Soc.*, 493, 4711, doi: [10.1093/mnras/staa414](https://doi.org/10.1093/mnras/staa414)
- van Haarlem, M. P., Wise, M. W., Gunst, A., et al. 2013, *Astronomy & astrophysics*, 556, A2, doi: [10.1051/0004-6361/201220873](https://doi.org/10.1051/0004-6361/201220873)
- Vedantham, H., Shankar, N. U., & Subrahmanyam, R. 2012, *Astrophys. J.*, 745, 176, doi: [10.1088/0004-637X/745/2/176](https://doi.org/10.1088/0004-637X/745/2/176)
- Wang, J., Santos, M. G., Bull, P., et al. 2021, *MNRAS*, 505, 3698, doi: [10.1093/mnras/stab1365](https://doi.org/10.1093/mnras/stab1365)
- Wolz, L., Abdalla, F. B., Blake, C., et al. 2014, *Mon. Not. Roy. Astron. Soc.*, 441, 3271, doi: [10.1093/mnras/stu792](https://doi.org/10.1093/mnras/stu792)
- Wolz, L., Abdalla, F. B., Alonso, D., et al. 2015, *PoS, AASKA14*, 035, doi: [10.22323/1.215.0035](https://doi.org/10.22323/1.215.0035)
- Yatawatta, S., et al. 2013, *Astron. Astrophys.*, 550, A136, doi: [10.1051/0004-6361/201220874](https://doi.org/10.1051/0004-6361/201220874)
- Yoshiura, S., et al. 2021, *Mon. Not. Roy. Astron. Soc.*, 505, 4775, doi: [10.1093/mnras/stab1560](https://doi.org/10.1093/mnras/stab1560)
- Zaroubi, S. 2013, *The Epoch of Reionization* (Berlin, Heidelberg: Springer Berlin Heidelberg), 45–101, doi: [10.1007/978-3-642-32362-1_2](https://doi.org/10.1007/978-3-642-32362-1_2)

APPENDIX

A. LOFAR RESULTS WITH $NS_{TH} + EOR$

Here we test the results of 1400 hours of LOFAR observations considering only the effect of ns_{th} . U-Net reaches optimal loss after 300 epochs. The 2D power spectra of the target **EoR** and the U-Net prediction result are shown on the left and right of Fig. 14, respectively. Their corresponding 2D cross power spectrum and 2D coherence power spectrum are displayed in Fig. 15. Although the target power spectrum and the power spectrum of the U-Net prediction result have similar shapes, they differ by an order of magnitude and have significant inconsistencies in the coherent power spectrum.

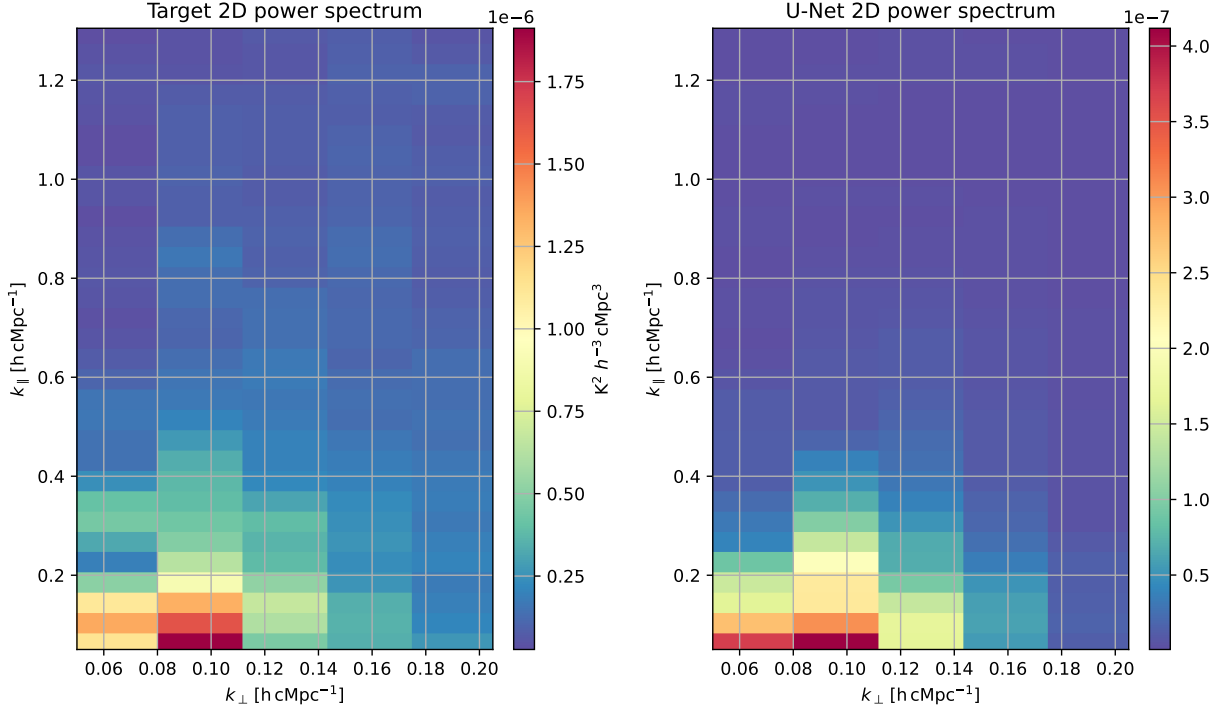


Figure 14. 2D power spectrum of the target **EoR** image and the 2D power spectrum of the predicted image given by U-Net after 300 epochs for LOFAR scenario when only consider ns_{th} .

B. LOFAR RESULTS WITH $NS_{EX} + NS_{TH} + EOR$

Here we add to the above the effect of ns_{ex} with 1400 hours of LOFAR observations. Due to the high intensity of ns_{th} and ns_{ex} , U-Net could not learn small-scale structures, so it reached the minimum loss after 300 epochs. Similarly, Fig. 16 illustrates the target 2D power spectrum and the 2D power spectrum of the U-Net results, and Fig. 17 shows their 2D cross power spectrum and 2D coherence power spectrum. Undoubtedly we get worse results, and on the 2D coherence power spectrum you can see that there is almost no correlation between the two images.

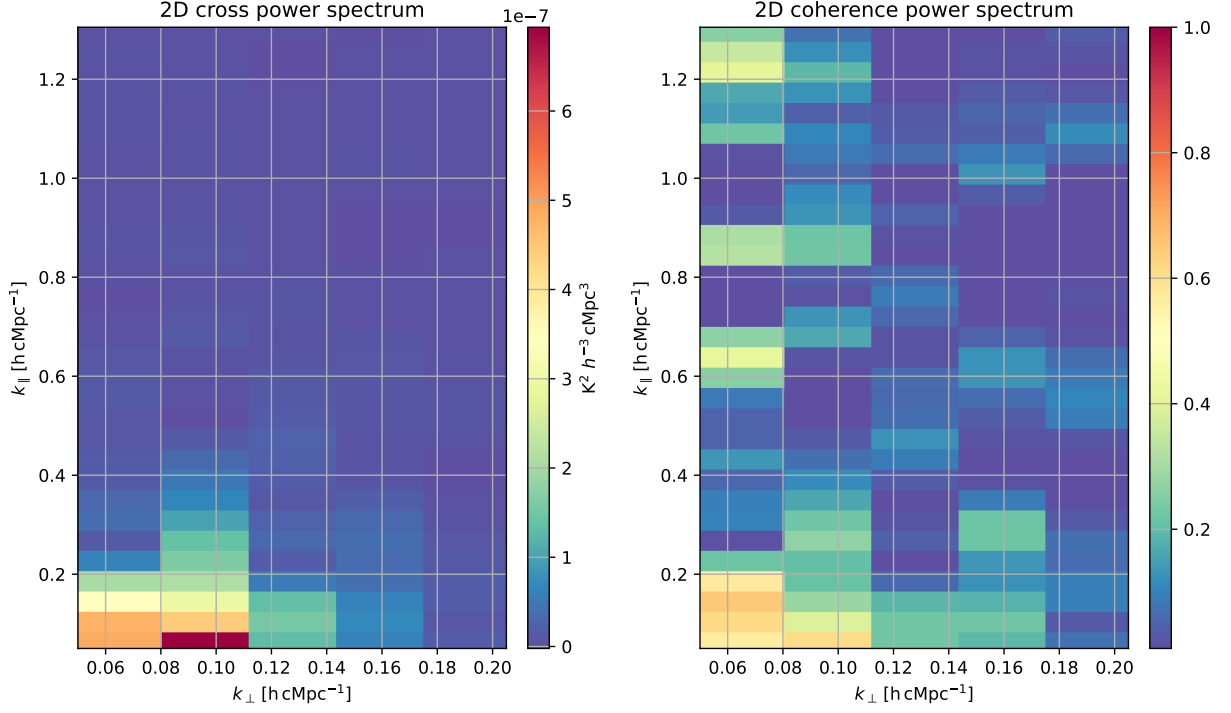


Figure 15. 2D cross power spectrum and 2D coherence power spectrum of the target and predicted images for LOFAR scenario when only consider ns_{th} .

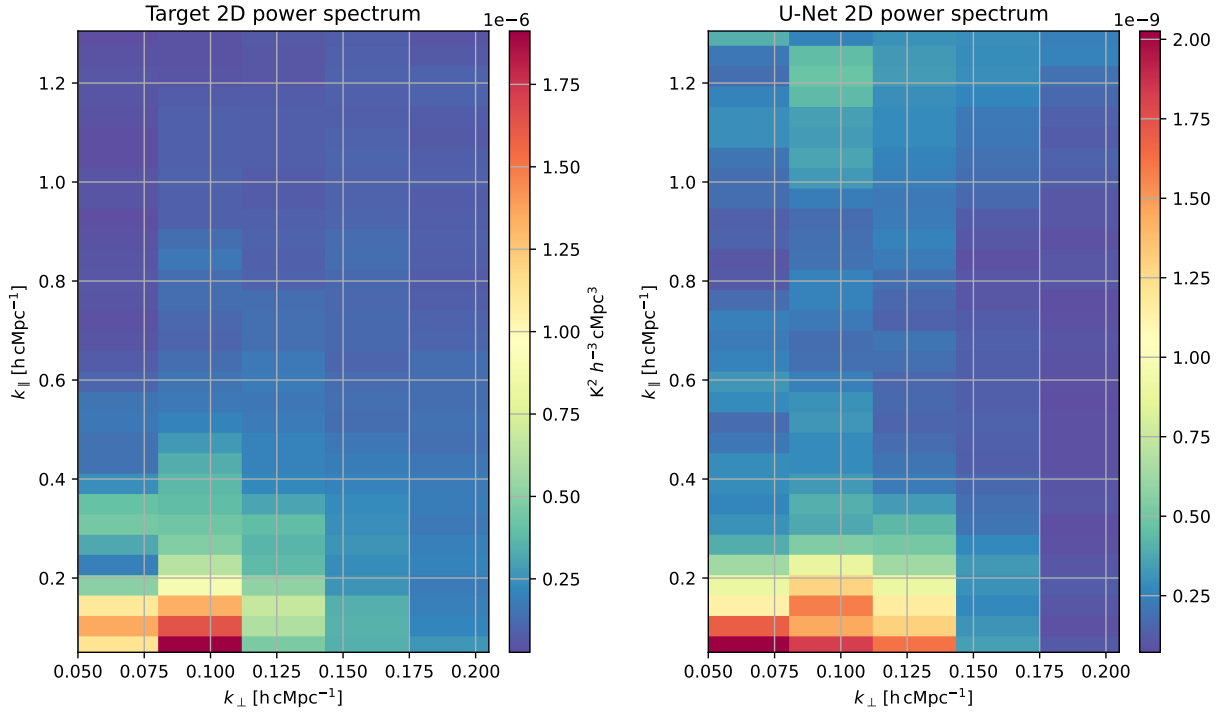


Figure 16. 2D power spectrum of the target **EoR** image and the 2D power spectrum of the predicted image given by U-Net after 500 epochs for LOFAR scenario when considering ns_{th} and ns_{ex} .

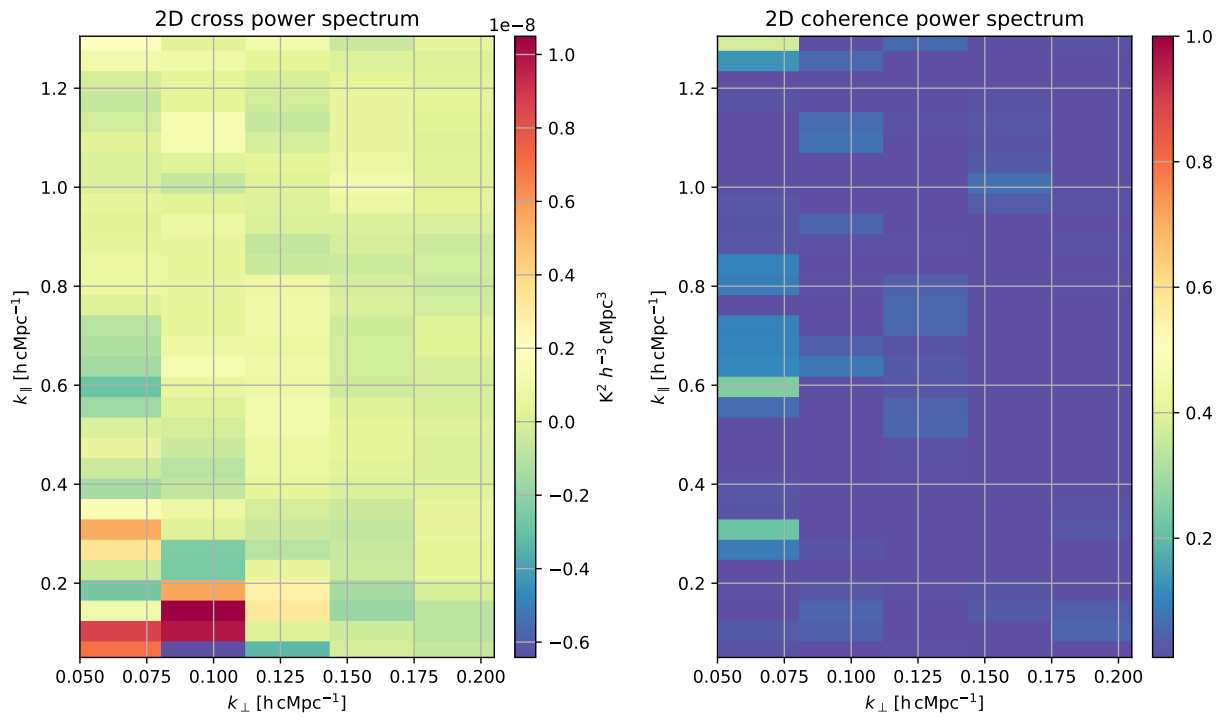


Figure 17. 2D cross power spectrum and 2D coherence power spectrum of the target and predicted images for LOFAR scenario when considering ns_{th} and ns_{ex} .